Conformational Motions and Water Networks at the #/# Interface in E. coli Ribonucleotide Reductase

HHS Public Access

Author manuscript

J Am Chem Soc. Author manuscript; available in PMC 2021 August 12.

Published in final edited form as:

J Am Chem Soc. 2020 August 12; 142(32): 13768–13778. doi:10.1021/jacs.0c04325.

Conformational Motions and Water Networks at the α/β Interface in *E. coli* Ribonucleotide Reductase

Clorice R. Reinhardt[1], **Pengfei Li**[2], **Gyunghoon Kang**[3,5], **JoAnne Stubbe**[4,5], **Catherine L. Drennan**[3,4,5,6], **Sharon Hammes-Schiffer**[2,6,*]

[1]Department of Molecular Biophysics and Biochemistry, Yale University, New Haven CT, USA

[2]Department of Chemistry, Yale University, New Haven CT, USA

[3]Howard Hughes Medical Institute, Massachusetts Institute of Technology, Cambridge MA, USA

[4]Department of Biology, Massachusetts Institute of Technology, Cambridge MA, USA

[5]Department of Chemistry, Massachusetts Institute of Technology, Cambridge MA, USA

[6]Fellow, Bio-inspired Solar Energy Program, Canadian Institute for Advanced Research (CIFAR), Toronto, ON M5G 1M1

Abstract

Ribonucleotide reductses (RNRs) catalyze the conversion of all four ribonucleotides to deoxyribonucleotides and are essential for DNA synthesis in all organisms. The active form of *E. coli* Ia RNR is composed of two homodimers that form the active α2β2 complex. Catalysis is initiated by long-range radical translocation over a ~32 Å proton-coupled electron transfer (PCET) pathway involving Y356β and Y731α at the interface. Resolving the PCET pathway at the α/β interface has been a long-standing challenge due to the lack of structural data. Herein molecular dynamics simulations based on a recently solved cryogenic-electron microscopy structure of an active α2β2 complex are performed to examine the structure and fluctuations of interfacial water, as well as the hydrogen-bonding interactions and conformational motions of interfacial residues along the PCET pathway. Our free energy simulations reveal that Y731 is able to sample both a flipped-out conformation, where it points toward the interface to facilitate interfacial PCET with Y356, and a stacked conformation with Y730 to enable collinear PCET with this residue. Y356 and Y731 exhibit hydrogen-bonding interactions with interfacial water molecules and, in some conformations, share a bridging water molecule, suggesting that the primary proton acceptor for PCET from Y356 and from Y731 is interfacial water. The conformational flexibility of Y731 and the hydrogen-bonding interactions of both Y731 and Y356 with interfacial water and hydrogen-bonded water chains appear critical for effective radical translocation along the PCET pathway. These simulations are consistent with biochemical and spectroscopic data and provide previously unattainable atomic-level insights into the fundamental mechanism of RNR.

*Corresponding author: sharon.hammes-schiffer@yale.edu.

Supporting Information

Computational details and supporting figures and tables (PDF)

Representative MD configuration for flipped-out Y731 (PDB)

Representative MD configuration for stacked Y731 (PDB)

Graphical Abstract

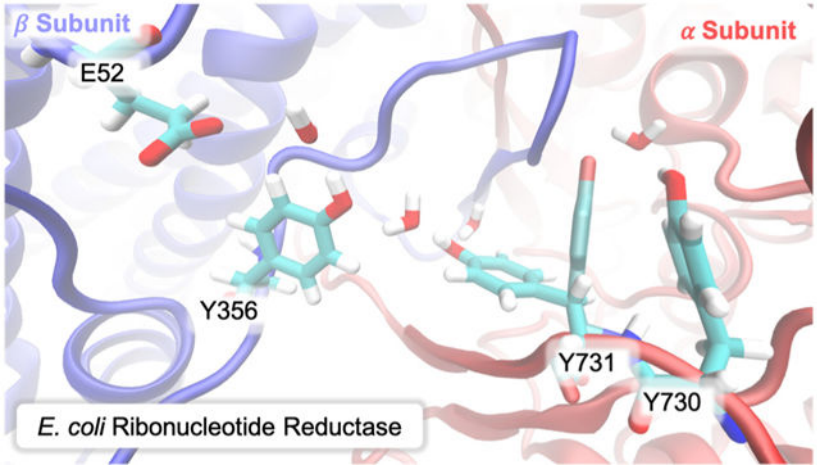

Introduction

Ribonucleotide reductases (RNRs) catalyze the conversion of all four ribonucleotides to deoxyribonucleotides and are essential enzymes for DNA synthesis.[1–3] Moreover, because RNR controls the relative concentrations of cellular deoxyribonucleotides, this enzyme also plays an important role in DNA replication and repair in all living organisms.[4] In *E. coli* and other class Ia RNRs, such as human and mouse, catalysis is initiated when a stable diferric-tyrosyl radical oxidizes a distal cysteine to a thiyl radical,[5] which abstracts a hydrogen atom from the bound ribonucleotide,[6–8] leading to a complex series of steps that ultimately produces the deoxyribonucleotide (Scheme 1). Allosteric specificity and activity effectors determine the substrate that will be reduced and the rate of this reduction, enabling RNR to maintain a balance of the deoxyribonucleotide pools within the cell.[9, 10] The long-range radical translocation over ~32 Å from the diferric-tyrosyl radical to the cysteine is proposed to occur through a series of proton-coupled electron transfer (PCET) reactions[11–15] involving tyrosine residues and purportedly a tryptophan residue. In general, oxidation of tyrosine decreases the p*K*a by ~12 units[16] and is typically associated with a concerted PCET mechanism, in which the proton is transferred to a nearby acceptor. Illumination of the overall PCET pathway and the mechanisms of the individual PCET steps in RNR has broad biochemical implications.

The active form of RNR, α2β2, is composed of two dimers: the α2 subunit, which contains the substrate and effector binding sites, and the β2 subunit, which contains the diferric-tyrosyl cofactor. Thus, the radical translocation pathway from the diferric-tyrosyl radical to the cysteine spans the β2 and the α2 subunits (Figure 1). This pathway, which was first proposed by Uhlin and Eklund using a docking model of α2 with β217 and later supported by mutagenesis studies,[2, 18, 19] has recently been structurally characterized by cryogenic electron microscopy (cryo-EM) to 3.6 Å resolution.[20] This structure of *E. coli* class Ia RNR, which was trapped in an α2β2 complex using a doubly substituted β2, E52Q/2,3,5-F3Y122-β2,[19] and wild type α2, has revealed the positioning of residues known and proposed to be part of this pathway:[20] Y122β↔[W48β] ↔Y356β ↔Y731α ↔Y730α ↔C439α. The

participation of these four tyrosine residues was established by perturbing their redox potentials with tyrosine analogs,[21–28] whereas the involvement of W48 in the PCET pathway has been proposed but has been more challenging to probe experimentally. The structure[20] (Figure 1) shows the four tyrosine residues and W48 lined up along this pathway, with ~10 Å distances between the tyrosines and bridging tryptophan in β, ~8 Å at the α/β interface between Y356β and Y731α, and ~3.5 Å in between the tyrosines and cysteine in α. These distances are consistent with PCET reactions being orthogonal to the pathway in the β2 subunit (i.e., the proton transfers to a residue or water molecule that is not along the electron transfer pathway) and collinear in the α2 subunit (i.e., the proton transfers to a residue along the electron transfer pathway).[2] The overall distance of radical transfer between Y122β and C439α to initiate catalysis is 32 Å, which is close to the distance predicted from spectroscopic studies of 35–38 Å.[26] This long distance is even more remarkable considering that the radical transfer occurs in both directions; upon completion of the conversion of the ribonucleotide to the deoxyribonucleotide, the reverse radical translocation process restores the diferric-tyrosyl radical.[29]

The availability of a structure of the active state of RNR[20] opens the door for computational analysis that was not possible previously. In particular, this structure has allowed for the visualization of the full β C-terminus, often referred to as the β-tail, which forms the α/β interface that affords the radical transfer between subunits. Twenty residues of this β-tail, including key PCET residue Y356, were disordered in all previous structures.[17, 30–35] This structure reveals that the β-tail stretches away from the core of β, runs deep into the α subunit, comes into contact with the substrate, makes a sharp turn at residues 348–350, and comes back toward β, inserting Y356β between W48β and Y731α to complete the PCET pathway, and finally wrapping around the α subunit and ending (Figure 1C). Although providing insights, previous computational studies on RNR were limited by the lack of structural information at the interface.[36–40]

With the structure of a trapped active state of RNR,[20] we can now begin to address a series of question about this long-range PCET process. A long-standing question has been whether the side chains of the tyrosines along the radical transfer pathway need to rearrange to enable PCET in the forward and reverse directions. More specifically, does the packing of the β-tail close to Y731α stabilize this residue in the observed stacked conformation with Y730α (Figure 1C), or is Y731α still able to rearrange (flip-out) as has been observed previously?[41, 42] Notably, the interconversion between the flipped-out and stacked conformations of Y731 has been shown to be within the timescale of turnover by spectroscopic studies on mutants,[43, 44] but it is unclear how the packing of the β-tail against Y731α might alter the behavior of this residue.

Another long-standing question has been the identities of the proton donors and acceptors for the interfacial PCET process involving Y356β and Y731α (Figure 1D). Two residues, E350β and E52β, have been proposed to serve as proton acceptors and/or be involved in the radical-transfer gating based on mutagenesis studies.[18, 19, 45, 46] One of these residues, E350β, is far from the PCET pathway[20] and appears to be important for anchoring the β-tail to the α subunit in the active state of RNR (Figure 1C). The other residue, E52β, is directly along the PCET pathway (Figure 1C), and its substitution to Q52 was key for the trapping of

active RNR for structural analysis.[19, 20] E52β is an excellent candidate for PT based on both its location and on the dramatic effect that its substitution has on the α2β2 complex stability,[19] but this residue appears to be too far from Y356 to be directly involved in PT. According to the cryo-EM structure,[20] no side chains appear to be close enough to PCET residue Y356 to directly transfer a proton. Therefore, either water molecules are involved in PT or side chains must rearrange. Although the resolution of the cryo-EM structure allows for visualization of side chains, it did not allow for the visualization of water molecules, leaving as unanswered the question of water structure surrounding the PCET residues. Questions about water structure and side chain movement are ideally suited for computational analysis.

The cryo-EM data of the asymmetric α2β2 structure[20] provides two test structures for molecular dynamics (MD) studies because one α subunit is in contact with a β subunit, forming an intact PCET pathway, whereas the other α subunit, which we will refer to as α', is not in contact with its partner β'. Biochemical analysis of the construct used in the cryo-EM structure determination showed that one product is produced per α2 dimer, indicating that one active site should be in a post-turnover state with the cysteines 225α and 462α oxidized, and the other active site should be in a pre-turnover state with the cysteines reduced and substrate bound.[20] The EM density indicates that the α' subunit is in the post-turnover state because a disulfide bond has formed and the β'-tail is disordered, whereas the α subunit appears to be trapped in the pre-turnover state with the substrate GDP bound, the effector TTP bound, and the β-tail ordered for PCET. Thus, this structure allows the simulation of the pre-turnover state with an intact PCET pathway between the α and β subunits, while also allowing comparison to the post-turnover state in the resolved regions of the α' and β' subunits.

Using this entire asymmetric cryo-EM structure as a starting point, we perform MD simulations to elucidate the entire PCET pathway, with particular emphasis directed at the previously elusive but critical interfacial region. Our MD simulations illustrate the conformational motions of the interfacial Y731α residue when the α subunit is interacting with the β subunit within an intact PCET pathway and when this interaction is absent for the α' subunit. These simulations also elucidate the structure and fluctuations of the interfacial water, as well as the hydrogen-bonding interactions with the interfacial residues. Moreover, these simulations provide insights into the primary proton acceptor for the two critical interfacial residues, Y356β and Y731α. The understanding about the PCET pathway obtained from these simulations will serve as the foundation for future mechanistic studies.

Methods

Molecular dynamics trajectories

The recently solved cryo-EM structure of the α2β2 complex using a doubly substituted β2 (E52Q/(2,3,5-F_3Y122)-β2) and WT α2, in the presence of bound substrate GDP and effector TTP, revealed an asymmetric structure, which consists of the active, interacting αβ pair and the inactive α′β′ pair. We used this structure as the basis for wild-type RNR simulations, reverting the mutated residues to their wild-type identities. In our simulations, the active αβ pair was modeled in the resting state (Fe2-OH2/Y•), and the inactive α′β′ pair was modeled in two different states, either the met state (Fe2-OH2/Y) or the state after radical

translocation (Fe2-OH/Y) to account for the uncertainty in the structure.[47] In all simulations, the second iron atom in the di-iron complex was modeled with a bound water molecule (Fe1-OH2). Our work uses the numbering present in the crystal structures, where Fe2 is the iron atom closest to Y122 and Fe1 is the distal iron atom.[20, 33] To examine the sensitivity of the results to the initial water configurations, we prepared the system using two different protocols: (1) adding water molecules according to the standard MD protocol, and (2) docking the water molecules resolved in the 5CI4 β2 crystal structure[33] into the active β subunit of the cryo-EM structure. The data from the simulations with two different initial water configurations, as well as those with the two different states of the metal cofactor in the β′ subunit, were found to be statistically equivalent in the analysis of the active αβ pair, and therefore the data were combined in the final analysis. For each system studied, three independent trajectories were propagated with different initial velocities. Table S1 summarizes the four systems studied herein, which corresponds to 12 independent 100 ns trajectories and a total of 1.2 μs of unbiased sampling.

The details about the system preparation, force field parameters, and equilibration are provided in the SI and are only briefly described here. The Amber ff14SB force field[48] was used to model the protein, and the TIP3P water model[49] was used to describe the solvent. The parameterization of the bound GDP and TTP molecules, as well as the tyrosine radical in the interacting β subunit, is described in the SI. The diiron metal center was parameterized using the MCPB.py utility[50] with AmberTools, and the Mg^{2+} ion coordinated to each of the TTP phosphate tails was treated with parameters from Ref.[51]. The atom types, partial charges, and optimized geometries for the RESP fittings are provided in Tables S2–S5.

All of the simulations started from the cryo-EM structure discussed above with hydrogen atoms added using the H++ webserver[52] at pH = 7.0, followed by manual adjustments for residues ligated to the metal centers (see SI). The system was solvated with TIP3P water molecules in a periodic cuboid box, and long-range electrostatic interactions were treated with the particle mesh Ewald method.[53] The net negative charge of the protein with bound nucleotides was neutralized with sodium ions, and additional Na^+ and Cl^- counterions were added to achieve a salt concentration of ~150 mM. Each solvated system contained ~300,000 atoms and was thoroughly equilibrated (Figure S1, Table S6). The root-mean square deviation (RMSD), for the C_α atoms in the wild-type systems averaged over all of the production trajectories was 2.2 – 2.6 Å with respect to the cryo-EM structure, and this average RMSD decreased to 1.4 – 1.5 Å if the lower-resolution α′β′ pair was excluded. The B-factors computed from the root-mean-square fluctuations in the MD simulations are qualitatively consistent with those of the cryo-EM structure (Figure S2). In general, MD simulations are limited by the accuracy of the potential energy surface, which is determined by the molecular mechanical force field in this case, and the amount of conformational sampling, which corresponds to the 12 independent 100 ns trajectories propagated herein. Given these limitations, the results depend strongly on the initial cryo-EM structure described in the Introduction.

The trajectories were visualized with the VMD program[54] and analyzed with the CPPTRAJ program[55] in AmberTools. The hydrogen-bonding interactions, inter-residue distances, and

solvent occupancy, and structure were analyzed for all trajectories. The hydrogen bonds were defined to have a heavy-atom distance less than or equal to 3.0 Å and a donor-hydrogen-acceptor angle greater than or equal to 135 degrees. The solvation shells around Y356, Y730, and Y731 were identified in terms of the distances between the tyrosine hydroxyl oxygen atom and water oxygen atoms with the first solvation shell defined as 3.4 Å. The radial distribution functions (RDFs) centered at the hydroxyl oxygen atoms of Y356, Y730, and Y731 were computed out to 30.0 Å with a grid spacing of 0.1 Å.

Umbrella Sampling of Y731 Motion

To investigate the conformational flexibility of Y731, we examined the motion of this residue in both the α and α′ chains for the WT enzyme (System #1 in Table S1) using umbrella sampling. Specifically, we generated the potential of mean force (PMF) along the χ1 angle (N-$C_α$-C ß-Cγ) of Y731. During the equilibration procedure for the MD trajectories described in the SI, after the harmonic restraints on the protein atoms were released, Y731α in the α2β2 structure flipped out, converting from the stacked conformation with χ1 ~ 271° found in the cryo-EM structure to a flipped-out conformation with χ1 ~ 180°. For each of the 12 independent 100 ns trajectories (i.e., three independent trajectories for each of the four systems defined in Table S1), it remained in this flipped-out conformation for the remainder of the trajectory. Because Y731α was in the flipped-out conformation for all of the equilibrated structures, and the umbrella sampling was started from the window corresponding to the flipped-out conformation, the simulations may have been biased toward this conformation. To address this issue, we also performed an independent set of umbrella sampling simulations with initial structures equilibrated to Y731α in the stacked conformation by applying a restraint on the dihedral angle during this equilibration.

These two independent sets of umbrella sampling simulations produced qualitatively similar but quantitatively different free energy profiles along the Y731α dihedral angle. Note that these two independent sets of umbrella sampling simulations differed only in their starting structures, with one starting in the flipped-out conformation and the other starting in the stacked conformation, but both sets sampled the entire range of the Y731α dihedral angle to describe the interconversion between the two conformations. Although sufficient local sampling is demonstrated for each set of simulations (Figure S3 and S4), the quantitative discrepancies most likely arise from differences in slow conformational changes from the β-tail loop and partially solvated interface. To ensure adequate sampling of the relevant β-tail conformations, we performed two-dimensional (2D) umbrella sampling simulations as a function of the original dihedral angle χ1 and an additional reaction coordinate describing the distance between P348:N and Y731:OH over the range 4.5 Å – 11.0 Å. The distance between Y731 and P348 was chosen as the second reaction coordinate because P348 is closest to Y731 in the cryo-EM structure, and a change in this distance describes the transition from a structure in which Y731 is packed tightly against the tip of the β-tail to a structure in which Y731 is further away. Moreover, P348 is a relatively rigid sidechain with no persistent sidechain hydrogen-bonding interactions and with limited ability to rotate, thereby avoiding complications in the interpretation of the resulting free energy surface. Additional details of the umbrella sampling simulations are given in the SI.

Results and Discussion

Prior to the recently solved cryo-EM structure of the active α2β2 complex,[20] the proposed PCET pathway lacked structural resolution because it traverses the interface between the α and β subunits (Figure 1). The identities of the residues at the interface were unknown, and the twenty residues of the β-tail that form much of the α/β interface had never been visualized in any structure. The α2β2 cryo-EM structure revealed the positions of these twenty residues and showed that the positions of other interfacial residues were predominantly consistent with those determined from structures of the individual subunits. Interfacial water structure and hydrogen-bond networks were not established, however, because the cryo-EM structure could not resolve water molecules. The average distances between residues along the proposed PCET pathway obtained from our MD simulations are in agreement with the corresponding distances in the cryo-EM structure (Table 1), with distances involving Y356 fluctuating the most. These greater fluctuations observed for Y356 are due mainly to the partially solvated interface and flexible nature of the β-tail on which Y356 resides. The total distance between the Y122 radical and the terminal pathway residue C439 is maintained during the MD simulations. This agreement between distances along the PCET pathway, as well as the RMSD values given above, provides validation for the simulated model protein system.

Conformational sampling of PCET residue Y731

As mentioned above, Y731α was observed to be in the stacked conformation in the cryo-EM structure but remained in the flipped-out conformation for each of the 12 independent 100 ns MD trajectories. In the flipped-out conformation, the Y731 side chain is pointed toward the interface, allowing greater interaction with interfacial water and Y356. This conformation has been observed in an aminotyrosine-substituted Y730 α2 structure (PDB code: 2XO4),[41] where this angle is measured as ~188° (Figure S5). A comparison of this X-ray crystallographic structure and the cryo-EM structure to flipped-out and stacked conformations obtained from our MD simulations is illustrated in Figure 2. In contrast to Y731α, the analogous Y in the α′ chain exhibits much more dynamic behavior in the MD simulations, oscillating between the flipped-out and stacked conformations. This behavior was observed across all of the independent trajectories (Figure S6).

We also performed additional simulations to ensure that the persistence of the flipped-out conformation for Y731α was not the result of biased initial conditions. When the system was equilibrated with a restraint applied to the dihedral angle of Y731α to maintain the stacked conformation ($\chi 1 \sim 271°$), the system remained stable in this conformation for ~20 ns and then exhibited greater fluctuations around the stacked conformation for another ~100 ns and eventually moved to the flipped-out conformation (Figure S7). These simulations do not provide information about the timescale of interconversion because of the restraints used to prepare the system and the observation of only a single interconversion. Moreover, as discussed above, Y731α remained in the flipped-out conformation in the combined 1.2 μs of unbiased MD simulations, preventing a direct measure of the timescale for interconversion. However, the combined unbiased MD trajectories do suggest that Y731α′ interconverts between the flipped-out and stacked conformation on the nanosecond timescale in the

absence of interactions with the β-tail, whereas this interconversion is significantly slower, possibly on the microsecond timescale, for Y731α in the presence of these interactions. Recent spectroscopic experiments indicate that Y731 is dynamic, interconverting between the stacked and flipped-out conformations on the nanosecond to microsecond timescale,[44, 46] which is faster than the enzyme turnover measured experimentally to be on the timescale of seconds (i.e., $2 – 10\ s^{-1}$).[9]

To explore the relative thermodynamic stabilities of the observed Y731 conformations, we performed umbrella sampling to compute the PMF as a function of the Y731 side chain dihedral angle, χ1. Altogether, over 5 μs of umbrella sampling was performed, exploring the dihedral angle for both Y731α and Y731α′. The one-dimensional PMF along the dihedral angle was generated from two independent sets of umbrella simulations starting from different equilibrated configurations corresponding to either the stacked or flipped-out conformation of Y731. In both cases, three free energy minima were observed, with the most favorable minimum corresponding to the flipped-out conformation with a dihedral angle of ~180°. Although they were qualitatively consistent, the two independently generated PMFs exhibited quantitative differences in the relative free energies of the minima (Figure S8), most likely due to limitations in conformational sampling of the slower motions, particularly in the β-tail region (Figure S9). Figure 3 depicts the PMF obtained by combining the data from both of these simulations for Y731α (blue solid curve). For comparison, the free energy profile for Y731α′, which does not interact with the β′ subunit, is also shown (green dashed curve).

As mentioned above, in the unbiased MD trajectories, Y731α was found to be relatively stable in the flipped-out conformation (χ1 ~ 182°), but Y731α′ was found to be much more mobile and to interconvert between the flipped-out and stacked conformations (χ1 ~ 170 − 300°) (see Figure S6). For the Y731α′ PMF, the region spanning 170 − 300° is nearly isoergic (Figure 3), consistent with the observation that all of these conformations are sampled during the unbiased 100 ns MD trajectories. Furthermore, the relative populations of the Y731α conformations are also consistent with the observations from the unbiased MD trajectories, where the flipped-out state was predominant. Note that the umbrella sampling simulations provide thermodynamic information about the relative free energies of the two conformations but do not provide quantitative information about the timescale because the PMF is computed along a specified reaction coordinate that may not correspond to the minimum free energy path. However, these simulations do allow a qualitative comparison between the PMFs for the two different subunits along the same reaction coordinate.

The observation that Y731 moves freely between the stacked and flipped-out conformations in the α′ subunit but not in the α subunit during the unbiased MD simulations, as well as the significantly higher free energy barrier observed in the PMF for the α subunit, suggests that the β-tail influences the kinetics for interconversion between these two conformations. Specifically, the interactions between Y731α and the β-tail may inhibit facile interconversion, although these interactions do not appear to prevent the interconversion altogether. The interactions between Y731α and the β-tail appear to be mainly of a steric nature, on the basis of the proximity of P348 and the lack of hydrogen-bonding interactions within 3.0 Å in the cryo-EM structure and in our simulations.

To further characterize this motion and explore the influence of the β-tail on the Y731 conformation, we generated a 2D PMF as a function of the dihedral angle and a second reaction coordinate describing the position of P348, near the tight turn of the β-tail, with respect to the Y731 hydroxyl oxygen (Figure 4, top). For the two-dimensional PMF (Figure 4, bottom), the lowest free energy minimum corresponds to the off-pathway conformation (dark purple), while the flipped-out and stacked conformations are ~5 kcal/mol higher in free energy but are isoergic with each other (i.e., within 0.2 kcal/mol). Although the umbrella sampling simulations do not provide reliable information about the minimum free energy pathways and the associated free energy barriers, the off-pathway conformation was never observed in any of the unrestrained MD trajectories, suggesting that the off-pathway conformation is most likely kinetically inaccessible in these simulations. The relative free energies of the flipped-out and stacked conformations of Y731 were computed to be ~4 kcal/mol from the 1D PMF and zero from the 2D PMF, illustrating the challenges associated with adequate conformational sampling for this large, flexible system. Nevertheless, all of these umbrella sampling simulations illustrate that both the flipped-out and stacked conformations observed in previous structural data are thermodynamically accessible at room temperature, even though the relative populations cannot be quantified because of sampling limitations.

As mentioned above, in the combined 1.2 μs of unbiased MD trajectories, Y731 remains predominantly in the flipped-out conformation, and even when it is equilibrated in the stacked conformation, it reverts to the flipped-out conformation in ~100 ns (Figure S7). Moreover, the 1D umbrella sampling simulations also suggest that the flipped-out conformation is more thermodynamically favorable, although the 2D umbrella sampling simulations suggest that they are nearly isoergic. Thus, the force field used in these simulations appears to favor the flipped-out conformation, even though the stacked conformation is observed in the cryo-EM structure. Several explanations may account for this apparent discrepancy. The force field may not be able to accurately describe the somewhat weak stacking interactions between Y730 and Y731, which is inherently quantum mechanical in nature. On the other hand, the doubly-substituted cryo-EM structure may be trapped in a state that does not correspond to the lowest free energy of the wild-type system as we modeled it. Both conformations have been observed in previous α2 crystal structures of RNR.[27, 41] Another possibility is that the relative populations of the stacked and flipped-out conformations could depend on the location of the radical along the PCET pathway, and this radical location may be different in the simulations versus the cryo-EM structure. Despite these uncertainties, the simulations demonstrate that both conformations of Y731α are thermodynamically accessible and that the relative populations are strongly influenced by interactions with the β-tail.

Hydrogen bonding along PCET pathway and with interfacial water

We also analyzed the hydrogen-bond network along the PCET pathway and the interfacial region between the α and β subunits. The hydrogen-bonding structure within the β subunit is similar to the structure described in the literature,[19] with a strong network of hydrogen bonds formed between D237, R236, Q43, and W48 (Table S7, Figure S11). The polar region adjacent to the tyrosyl radical at Y122 is relatively immobile, as shown by the persistence of

a significant number of hydrogen bonds and small fluctuations in the Y122-W48 distance (Table 1, standard deviation of 0.3 Å). In contrast, at the αβ interface, Y356 does not form persistent hydrogen bonds with the surrounding side chains, hydrogen bonding to R411α and N322α with a frequency less than <5% across the MD trajectories. In addition, Y356 interacts with E52 within the β subunit by forming a direct hydrogen bond (Figure S12) or interacting through a bridging water molecule (Figure 5) for 18% and 9%, respectively, of the combined MD trajectories (Table S7). Notably, we find that E52β can adopt multiple positions, corroborating the previous observations in the literature suggesting the ability of this residue to sample multiple conformations.[19, 20] The mobility of E52 and other interfacial residues is evident by the root-mean-square fluctuations (Table S8), which indicate that E52, Y356, and Y731 are 3−5 times more mobile in comparison to W48.

Although E52 can hydrogen bond directly to Y356, the most frequent hydrogen-bonding partners of Y356 are water molecules located in the interfacial region between the α and β subunits. Previous modeling of EPR spectra suggests that two symmetrical, exchangeable, hydrogen bonded water molecules could reproduce the perturbed g_x tensor of Y356•,[56] although the mechanistic roles of these water molecules are unclear. This modeling also suggested that a single water molecule and a hydrogen bond from a protein residue could produce a similar shift, although less likely. The possibilities discussed in the context of modeling the EPR data are consistent with the variety of conformations observed in our MD simulations. Consistent with this previous work, we observed an average of 1.5 ± 0.8 water molecules with oxygen atoms within 3.4 Å of the Y356 oxygen atom (Table S9). In the majority of conformations sampled from the combined MD trajectories, two water molecules satisfied this criterion (Figures 5 and 6).

In some conformations sampled during the MD trajectories, Y356 was found to share bridging waters with Y731 and/or E52, although these interactions fluctuate due to the dynamic nature of the solvated interface. In some cases, a chain of two hydrogen-bonded water molecules was found between E52 and Y356, or a chain of hydrogen-bonded water molecules was observed to lead from Y356 to bulk water (Figure 5). The solvent structure around Y356 was also analyzed by computing the radial distribution function (RDF) between the tyrosine hydroxyl oxygen atom and surrounding water molecules (Figure 7, dark blue curve). Y356 exhibits a relatively broad peak for the first solvation shell because of the probability of two simultaneous hydrogen-bonding interactions at the solvated interface. Thus, the MD simulations suggest that the proton acceptor for Y356 is a water molecule in the interfacial region, and presumably this proton is subsequently shuttled to bulk solvent. Water networks allowing redox active enzymes to shuttle protons to solvent have also been characterized computationally in other proteins.[57, 58]

Previously, Y356 and Y731 were proposed to communicate across the interface on the basis of EPR experiments indicating that the local environment around Y356 is influenced by Y731 via mutation studies.[56] However, a direct hydrogen bond between these two residues is not supported by H^1 ENDOR data[44] or the distances in the cryo-EM structure.[20] We did not observe a direct hydrogen bond between Y356 and Y731 in our MD simulations, but a bridging water molecule was found between Y356 and Y731 in the flipped-out conformation for 6% of the combined MD trajectories (Figure 5). The presence of this bridging water

depends on the relative orientation of Y356 and Y731 and thus was observed with a frequency of 25% for two of the 100 ns MD trajectories and not at all for some of the other MD trajectories. Y731 exhibited a hydrogen bond with at least one water molecule for 97% of the combined unbiased MD trajectories, for which Y731 was predominantly in the flipped-out conformation (Table S10). Moreover, for the majority of conformations sampled, Y731 was found to have two water molecules in the vicinity of its oxygen atom (Figures 5 and 6). Note that analysis of the stacked Y731 conformations obtained from the MD trajectory equilibrated with a restraint on the Y731 dihedral angle maintaining the stacked conformation decreased the percentage of hydrogen bonding with at least one water molecule from 97% to 84% (Figure S7, Table S10).

To further interrogate the local water environment of Y730 and Y731, we computed the RDFs of Y731 and Y730 with respect to the surrounding water molecules for the combined MD trajectories with Y731 predominantly in the flipped-out conformation (Figure 7). Similar to Y356, the RDF for Y731 exhibits a strong but slightly narrower peak for the first solvation shell, with an average of 1.8 water molecules within 3.4 Å. In contrast, Y730 exhibits a sharp peak for the first solvation shell, and then the RDF quickly decays to zero before rising again. This behavior arises because Y730 is not located at the interface, and the water molecule hydrogen bonded to this residue is not readily exchangeable. As a result, Y730 maintains a persistent, strong hydrogen bond to a single water molecule (i.e., a hydrogen bond with a donor-acceptor distance < 3.0 Å persists for 94% of the combined trajectories) and occasionally interacts with Q349 (Table S10). The interaction with this water molecule is consistent with structural[17, 27, 59] and spectroscopic data,[27] but an additional water molecule may also be located nearby, as evident by the average of 1.3 water molecules within 3.4 Å (Table S9).

Conformational gating of PCET afforded by E350 interactions

The β-tail residue E350 has been extensively studied,[18, 25, 43, 46] with the recent analyses indicating that E350 plays an essential role in the conformational gating of PCET.[40] The cryo-EM structure suggested how E350 might contribute to the establishment of the PCET pathway, revealing that E350 interacts with two residues of the α subunit, K154α and S647α, which would serve to support the tight turn that the β-tail makes underneath the substrate-binding site. To further examine the role of E350, we analyzed its interactions over the MD trajectories in the α2β2 systems. In our α2β2 MD simulations, E350β retains a salt bridge with K154α throughout the trajectories and forms a hydrogen bond with S647α for 25% of the MD trajectories (Figure 8 and Table S11). The maintenance of these interactions is consistent with the observed interactions in the cryo-EM structure and corroborates the proposal that E350 aligns the interface for PCET.[20] In particular, weakening of these interactions would affect the β-tail positioning and could thereby impact the positioning and flexibility of Y731α. As discussed above, our MD simulations show that interconversion between the stacked and flipped-out conformations is significantly influenced by interactions with the β-tail.

Conclusions

Our MD simulations based on the recently solved *E. coli* RNR α2β2 cryo-EM structure have elucidated the conformational flexibility of interfacial residues, the hydrogen-bonding interactions along the 32 Å PCET pathway, and the role of water in the interfacial region. The PCET reaction between Y731α and Y730α is thought to require a stacked conformation between these two tyrosine residues to enable collinear proton transfer between them, but the interfacial PCET reaction between Y356β and Y731α is less understood because the proton transfer is presumed to be orthogonal to the PCET pathway. Our free energy simulations illustrate that Y731α is flexible enough to sample the flipped-out conformation, in which it is pointing toward the interface, as well as the stacked conformation. The relative free energies of the stacked and flipped-out conformations are sufficiently similar to enable both to be populated at room temperature. This conformational flexibility of Y731α, even when it is closely associated with the β subunit, could be important for allowing this residue to participate in both forward and reverse PCET reactions. Moreover, our simulations imply that the interactions of Y731α with the β subunit impact the mobility of this residue, as well as the interconversion between and the relative populations of the two different conformations.

These simulations also suggest that interfacial PCET involves proton transfer to and from water molecules. Typically, Y356β forms hydrogen bonds with two water molecules that can be shared as a bridging water molecule or bridging hydrogen-bonded water chain with E52β and/or Y731α in some cases. Although E52β is conformationally flexible enough to adjust to a position that is capable of direct hydrogen bonding with Y356β, the much higher prevalence of water compared to E52 for exhibiting hydrogen-bonding interactions with Y356 in our MD simulations supports water as a more likely candidate for the proton acceptor from Y356β. However, E52β cannot be completely ruled out as a possible proton acceptor. Furthermore, Y731α is almost always hydrogen bonded to at least one interfacial water molecule and is often hydrogen bonded to two of them in the flipped-out conformation, suggesting that PCET from Y731α, which entails interfacial electron transfer to Y356β, is accompanied by proton transfer to an interfacial water molecule. The conformational flexibility of Y731α at the interface, combined with hydrogen-bonding interactions with interfacial water, may be important for effective radical transfer along the PCET pathway.

These simulations are consistent with previous biochemical and spectroscopic data and provide atomic-level insights that were not attainable prior to the recently solved cryo-EM structure of the active complex. However, these simulations most likely do not describe many of the slower, potentially rate-limiting conformational changes and do not explore the chemical steps along the PCET pathway. Nevertheless, this work forms the foundation for future investigations of the individual PCET reactions as we strive to understand this remarkably long radical transfer process. The mouse, human, and *E. coli* class Ia RNRs share the same active site chemistry and effector specificity and the same PCET pathway residues.[60] All of these RNRs also exhibit asymmetric and dynamic interactions between the subunits. Thus, the PCET pathway associated with radical transfer in *E. coli* RNR is

generalizable to the mouse and human Ia RNRs. Moreover, understanding the subtle differences between human and bacterial RNRs could have therapeutic implications.

Supplementary Material

Refer to Web version on PubMed Central for supplementary material.

Acknowledgements

This work was supported by the National Institutes of Health Grant Number GM056207 (S.H-S.) and R35 GM126982 (C.L.D). C.L.D is an HHMI Investigator. C.L.D and S.H-S. are fellows of the Bio-inspired Solar Energy Program, Canadian Institute for Advanced Research. C.R.R was supported by the National Science Foundation Graduate Research Fellowship Program under Grant No. DGE1752134 and in part by the National Institutes of Health (5T32GM06754 3-12). G.K. was supported by a David H. Koch Graduate Fellowship. This work utilized the Extreme Science and Engineering Discovery Environment (XSEDE), which is supported by the National Science Foundation (grant number ACI-1548562).[61] In particular, GPU resources of the Comet supercomputer at San Diego Supercomputer Center were used (allocation number TG-CHE190044). Computational resources of the Yale Center for Research Computing (YCRC) were used for processing trajectories.

References

(1). Stubbe J; Nocera DG; Yee CS; Chang MCY, Radical Initiation in the Class I Ribonucleotide Reductase: Long-Range Proton-Coupled Electron Transfer? Chem. Rev 2003, 103, 2167–2202. [PubMed: 12797828]

(2). Minnihan EC; Nocera DG; Stubbe J, Reversible, Long-Range Radical Transfer in E. coli Class Ia Ribonucleotide Reductase. Acc. Chem. Res 2013, 46, 2524–2535. [PubMed: 23730940]

(3). Stubbe J; van Der Donk WA, Protein Radicals in Enzyme Catalysis. Chem Rev 1998, 98, 705–762. [PubMed: 11848913]

(4). Hofer A; Crona M; Logan DT; Sjöberg B-M, DNA building blocks: keeping control of manufacture. Crit. Rev. Biochem. Mol. Biol 2012, 47, 50–63. [PubMed: 22050358]

(5). Bennati M; Robblee JH; Mugnaini V; Stubbe J; Freed JH; Borbat P, EPR Distance Measurements Support a Model for Long-Range Radical Initiation in E. coli Ribonucleotide Reductase. J. Am. Chem. Soc 2005, 127, 15014–15015. [PubMed: 16248626]

(6). Stubbe J; Ackles D, On the mechanism of ribonucleoside diphosphate reductase from Escherichia coli. Evidence for 3'-C--H bond cleavage. J. Biol. Chem 1980, 255, 8027–8030. [PubMed: 6997288]

(7). Stubbe J; Ator M; Krenitsky T, Mechanism of ribonucleoside diphosphate reductase from Escherichia coli. Evidence for 3'-C--H bond cleavage. J. Biol. Chem 1983, 258, 1625–1631. [PubMed: 6337142]

(8). Olshansky L; Pizano AA; Wei Y; Stubbe J; Nocera DG, Kinetics of Hydrogen Atom Abstraction from Substrate by an Active Site Thiyl Radical in Ribonucleotide Reductase. J. Am. Chem. Soc 2014, 136, 16210–16216. [PubMed: 25353063]

(9). Ge J; Yu G; Ator MA; Stubbe J, Pre-steady-state and steady-state kinetic analysis of E. coli class I ribonucleotide reductase. Biochemistry 2003, 42, 10071–10083. [PubMed: 12939135]

(10). Greene BL; Nocera DG; Stubbe J, Basis of dATP inhibition of RNRs. J. Biol. Chem 2018, 293, 10413–10414. [PubMed: 29959279]

(11). Hammes-Schiffer S, Theoretical perspectives on proton-coupled electron transfer reactions. Acc. Chem. Res 2001, 34, 273–281. [PubMed: 11308301]

(12). Huynh MHV; Meyer TJ, Proton-coupled electron transfer. Chem. Rev 2007, 107, 5004–5064. [PubMed: 17999556]

(13). Hammes-Schiffer S; Stuchebrukhov AA, Theory of coupled electron and proton transfer reactions. Chem. Rev 2010, 110, 6939–6960. [PubMed: 21049940]

(14). Warren JJ; Tronic TA; Mayer JM, Thermochemistry of Proton-Coupled Electron Transfer Reagents and its Implications. Chem. Rev 2010, 110, 6961–7001. [PubMed: 20925411]

(15). Glover SD; Jorge C; Liang L; Valentine KG; Hammarstrom L; Tommos C, Photochemical tyrosine oxidation in the structurally well-defined alpha3Y protein: proton-coupled electron transfer and a long-lived tyrosine radical. J. Am. Chem. Soc 2014, 136, 14039–14051. [PubMed: 25121576]

(16). Dixon WT; Murphy D, Determination of the acidity constants of some phenol radical cations by means of electron spin resonance. J. Chem. Soc., Faraday Trans. 2 1976, 72, 1221–1230.

(17). Uhlin U; Eklund H, Structure of ribonucleotide reductase protein R1. Nature 1994, 370, 533–539. [PubMed: 8052308]

(18). Climent I; Sjoeberg BM; Huang CY, Site-directed mutagenesis and deletion of the carboxyl terminus of Escherichia coli ribonucleotide reductase protein R2. Effects on catalytic activity and subunit interaction. Biochemistry 1992, 31, 4801–4807. [PubMed: 1591241]

(19). Lin Q; Parker MJ; Taguchi AT; Ravichandran K; Kim A; Kang G; Shao J; Drennan CL; Stubbe J, Glutamate 52-beta at the alpha/beta subunit interface of Escherichia coli class Ia ribonucleotide reductase is essential for conformational gating of radical transfer. J. Biol. Chem 2017, 292, 9229–9239. [PubMed: 28377505]

(20). Kang G; Taguchi AT; Stubbe J; Drennan CL, Structure of a trapped radical transfer pathway within a ribonucleotide reductase holocomplex. Science 2020, 368, 424–427.

(21). Yee CS; Seyedsayamdost MR; Chang MCY; Nocera DG; Stubbe J, Generation of the R2 Subunit of Ribonucleotide Reductase by Intein Chemistry: Insertion of 3-Nitrotyrosine at Residue 356 as a Probe of the Radical Initiation Process. Biochemistry 2003, 42, 14541–14552. [PubMed: 14661967]

(22). Yee CS; Chang; Ge J; Nocera DG; Stubbe J, 2,3-Difluorotyrosine at Position 356 of Ribonucleotide Reductase R2: A Probe of Long-Range Proton-Coupled Electron Transfer. J. Am. Chem. Soc 2003, 125, 10506–10507. [PubMed: 12940718]

(23). Seyedsayamdost MR; Stubbe J, Site-Specific Replacement of Y356 with 3,4-Dihydroxyphenylalanine in the β2 Subunit of E. coli Ribonucleotide Reductase. J. Am. Chem. Soc 2006, 128, 2522–2523. [PubMed: 16492021]

(24). Seyedsayamdost MR; Reece SY; Nocera DG; Stubbe J, Mono-, Di-, Tri-, and Tetra-Substituted Fluorotyrosines: New Probes for Enzymes That Use Tyrosyl Radicals in Catalysis. J. Am. Chem. Soc 2006, 128, 1569–1579. [PubMed: 16448128]

(25). Seyedsayamdost MR; Yee CS; Reece SY; Nocera DG; Stubbe J, pH Rate Profiles of FnY356−R2s (n = 2, 3, 4) in Escherichia coli Ribonucleotide Reductase: Evidence that Y356 Is a Redox-Active Amino Acid along the Radical Propagation Pathway. J. Am. Chem. Soc 2006, 128, 1562–1568. [PubMed: 16448127]

(26). Seyedsayamdost MR; Chan CTY; Mugnaini V; Stubbe J; Bennati M, PELDOR Spectroscopy with DOPA-β2 and NH2Y-α2s: Distance Measurements between Residues Involved in the Radical Propagation Pathway of E. coli Ribonucleotide Reductase. J. Am. Chem. Soc 2007, 129, 15748–15749. [PubMed: 18047343]

(27). Yokoyama K; Uhlin U; Stubbe J, Site-Specific Incorporation of 3-Nitrotyrosine as a Probe of pKa Perturbation of Redox-Active Tyrosines in Ribonucleotide Reductase. J. Am. Chem. Soc 2010, 132, 8385–8397. [PubMed: 20518462]

(28). Ravichandran KR; Taguchi AT; Wei Y; Tommos C; Nocera DG; Stubbe J, A >200 meV Uphill Thermodynamic Landscape for Radical Transport in Escherichia coli Ribonucleotide Reductase Determined Using Fluorotyrosine-Substituted Enzymes. J. Am. Chem. Soc 2016, 138, 13706–13716. [PubMed: 28068088]

(29). Seyedsayamdost MR; Stubbe J, Forward and Reverse Electron Transfer with the Y356DOPA-β2 Heterodimer of E. coli Ribonucleotide Reductase. J. Am. Chem. Soc 2007, 129, 2226–2227. [PubMed: 17279757]

(30). Nordlund P; Sjöberg B-M; Eklund H, Three-dimensional structure of the free radical protein of ribonucleotide reductase. Nature 1990, 345, 593–598. [PubMed: 2190093]

(31). Nordlund P; Eklund H, Structure and function of the Escherichia coli ribonucleotide reductase protein R2. J. Mol. Biol 1993, 232, 123–164. [PubMed: 8331655]

(32). Sommerhalter M; Saleh L; Bollinger JM Jr.; Rosenzweig AC, Structure of Escherichia coli ribonucleotide reductase R2 in space group P6122. Acta Crystallogr., Sect. D: Biol. Crystallogr 2005, 61, 1649–1654. [PubMed: 16301799]

(33). Oyala PH; Ravichandran KR; Funk MA; Stucky PA; Stich TA; Drennan CL; Britt RD; Stubbe J, Biophysical characterization of fluorotyrosine probes site-specifically incorporated into enzymes: E. coli ribonucleotide reductase as an example. J. Am. Chem. Soc 2016, 138, 7951–7964. [PubMed: 27276098]

(34). Ando N; Brignole EJ; Zimanyi CM; Funk MA; Yokoyama K; Asturias FJ; Stubbe J; Drennan CL, Structural interconversions modulate activity of Escherichia coli ribonucleotide reductase. Proc. Natl. Acad. Sci. U. S. A 2011, 108, 21046–21051. [PubMed: 22160671]

(35). Zimanyi CM; Ando N; Brignole EJ; Asturias FJ; Stubbe J; Drennan CL, Tangled up in knots: structures of inactivated forms of E. coli class Ia ribonucleotide reductase. Structure 2012, 20, 1374–1383. [PubMed: 22727814]

(36). Siegbahn PEM; Eriksson L; Himo F; Pavlov M, Hydrogen Atom Transfer in Ribonucleotide Reductase (RNR). J. Phys. Chem. B 1998, 102, 10622–10629.

(37). Cerqueira NM; Fernandes PA; Eriksson LA; Ramos MJ, Ribonucleotide activation by enzyme ribonucleotide reductase: understanding the role of the enzyme. J. Comput. Chem 2004, 25, 2031–2037. [PubMed: 15481089]

(38). Han WG; Sandala GM; Giammona DA; Bashford D; Noodleman L, Mossbauer properties of the diferric cluster and the differential iron(II)-binding affinity of the iron sites in protein R2 of class Ia Escherichia coli ribonucleotide reductase: a DFT/electrostatics study. Dalton Trans. 2011, 40, 11164–11175. [PubMed: 21837345]

(39). Kaila VRI; Hummer G, Energetics of Direct and Water-Mediated Proton-Coupled Electron Transfer. J. Am. Chem. Soc 2011, 133, 19040–19043. [PubMed: 21988482]

(40). Migliore A; Polizzi NF; Therien MJ; Beratan DN, Biochemistry and Theory of Proton-Coupled Electron Transfer. Chem. Rev 2014, 114, 3381–3465. [PubMed: 24684625]

(41). Minnihan EC; Seyedsayamdost MR; Uhlin U; Stubbe J, Kinetics of radical intermediate formation and deoxynucleotide production in 3-aminotyrosine-substituted Escherichia coli ribonucleotide reductases. J. Am. Chem. Soc 2011, 133, 9430–9440. [PubMed: 21612216]

(42). Uppsten M; Färnegårdh M; Jordan A; Eliasson R; Eklund H; Uhlin U, Structure of the Large Subunit of Class Ib Ribonucleotide Reductase from Salmonella typhimurium and its Complexes with Allosteric Effectors. J. Mol. Biol 2003, 330, 87–97. [PubMed: 12818204]

(43). Greene BL; Taguchi AT; Stubbe J; Nocera DG, Conformationally Dynamic Radical Transfer within Ribonucleotide Reductase. J. Am. Chem. Soc 2017, 139, 16657–16665. [PubMed: 29037038]

(44). Kasanmascheff M; Lee W; Nick TU; Stubbe J; Bennati M, Radical transfer in E coli ribonucleotide reductase: a NH2Y731/R411A-α mutant unmasks a new conformation of the pathway residue 731. Chem. Sci 2016, 7, 2170–2178. [PubMed: 29899944]

(45). Climent I; Sjoeberg BM; Huang CY, Carboxyl-terminal peptides as probes for Escherichia coli ribonucleotide reductase subunit interaction: kinetic analysis of inhibition studies. Biochemistry 1991, 30, 5164–5171. [PubMed: 2036382]

(46). Ravichandran K; Minnihan EC; Lin Q; Yokoyama K; Taguchi AT; Shao J; Nocera DG; Stubbe J, Glutamate 350 Plays an Essential Role in Conformational Gating of Long-Range Radical Transport in Escherichia coli Class Ia Ribonucleotide Reductase. Biochemistry 2017, 56, 856–868. [PubMed: 28103007]

(47). Wörsdörfer B; Conner DA; Yokoyama K; Livada J; Seyedsayamdost M; Jiang W; Silakov A; Stubbe J; Bollinger JM Jr.; Krebs C, Function of the diiron cluster of Escherichia coli class Ia ribonucleotide reductase in proton-coupled electron transfer. J. Am. Chem. Soc 2013, 135, 8585–8593. [PubMed: 23676140]

(48). Maier JA; Martinez C; Kasavajhala K; Wickstrom L; Hauser KE; Simmerling C, ff14SB: improving the accuracy of protein side chain and backbone parameters from ff99SB. J. Chem. Theory Comput 2015, 11, 3696–3713. [PubMed: 26574453]

(49). Jorgensen WL; Chandrasekhar J; Madura JD; Impey RW; Klein ML, Comparison of simple potential functions for simulating liquid water. J. Chem. Phys 1983, 79, 926–935.

(50). Li P; Merz KM Jr, MCPB.py: A Python Based Metal Center Parameter Builder. J. Chem. Inf. Model 2016, 56, 599–604. [PubMed: 26913476]

(51). Allnér O; Nilsson L; Villa A, Magnesium Ion–Water Coordination and Exchange in Biomolecular Simulations. J. Chem. Theory Comput 2012, 8, 1493–1502. [PubMed: 26596759]

(52). Gordon JC; Myers JB; Folta T; Shoja V; Heath LS; Onufriev A, H++: a server for estimating pKas and adding missing hydrogens to macromolecules. Nucleic Acids Res. 2005, 33, W368–W371. [PubMed: 15980491]

(53). Darden T; York D; Pedersen L, Particle mesh Ewald: An N log(N) method for Ewald sums in large systems. J. Chem. Phys 1993, 98, 10089–10092.

(54). Humphrey W; Dalke A; Schulten K, VMD: visual molecular dynamics. J. Mol. Graph 1996, 14, 33–8, 27–8. [PubMed: 8744570]

(55). Roe DR; Cheatham TE, PTRAJ and CPPTRAJ: Software for Processing and Analysis of Molecular Dynamics Trajectory Data. J. Chem. Theory Comput 2013, 9, 3084–3095. [PubMed: 26583988]

(56). Nick TU; Ravichandran KR; Stubbe J; Kasanmascheff M; Bennati M, Spectroscopic Evidence for a H Bond Network at Y356 Located at the Subunit Interface of Active E. coli Ribonucleotide Reductase. Biochemistry 2017, 56, 3647–3656. [PubMed: 28640584]

(57). Farahvash A; Stuchebrukhov A, Investigating the Many Roles of Internal Water in Cytochrome c Oxidase. J. Phys. Chem. B 2018, 122, 7625–7635. [PubMed: 30011995]

(58). de la Lande A; Babcock NS; Řezáč J; Sanders BC; Salahub DR, Surface residues dynamically organize water bridges to enhance electron transfer between proteins. Proc. Natl. Acad. Sci. U. S. A 2010, 107, 11799–11804. [PubMed: 20547871]

(59). Eriksson M; Uhlin U; Ramaswamy S; Ekberg M; Regnstrom K; Sjoberg BM; Eklund H, Binding of allosteric effectors to ribonucleotide reductase protein R1: reduction of active-site cysteines promotes substrate binding. Structure 1997, 5, 1077–1092. [PubMed: 9309223]

(60). Cotruvo JA; Stubbe J, Class I ribonucleotide reductases: metallocofactor assembly and repair in vitro and in vivo. Annu. Rev. Biochem 2011, 80, 733–767. [PubMed: 21456967]

(61). Towns J; Cockerill T; Dahan M; Foster I; Gaither K; Grimshaw A; Hazlewood V; Lathrop S; Lifka D; Peterson GD, XSEDE: accelerating scientific discovery. Comput. Sci. Eng 2014, 16, 62–74.

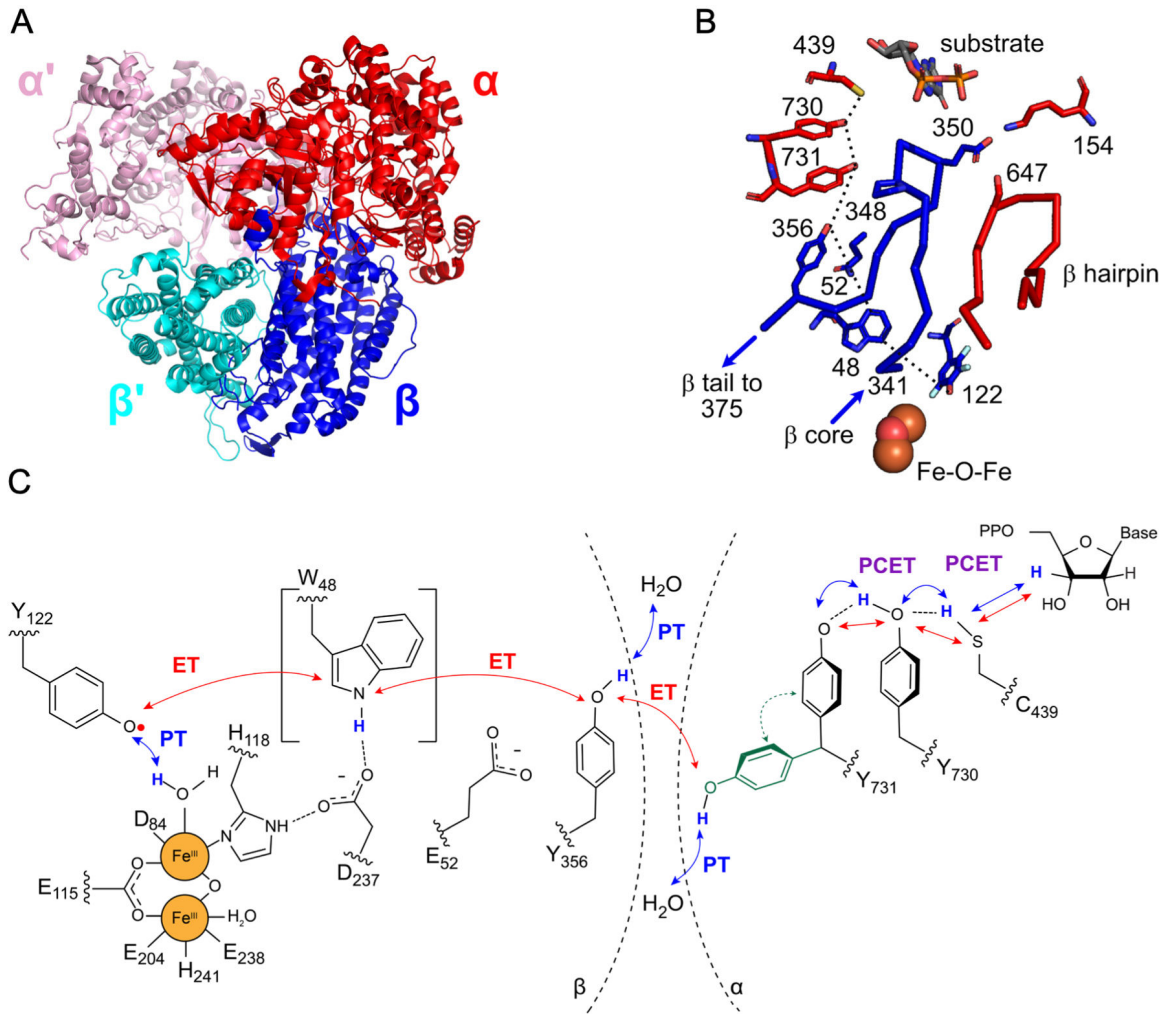

Figure 1.

Schematic depiction of the reaction catalyzed by RNR and visualization of the radical pathway. A) The cryo-EM structure of the $\alpha_2\beta_2$ complex reveals asymmetry: the αβ interacting pair (red and dark blue) is trapped in a pre-turnover state with the PCET pathway intact, whereas the α′β′ (lavender and cyan) pair appears to be in a post-turnover state with the β′ tail dissociated. B) Visualization of the PCET pathway residues and the β-tail loop with α in red and β in blue. C) The proposed ~32 Å PCET pathway in RNR: Y122β↔ [W48β] ↔Y356β ↔Y731α ↔Y730α ↔C439α and proposed proton transfers to water at the interface and putative conformational change of Y731 in dark green. For simplicity, this figure does not show the full mechanism of nucleotide reduction.

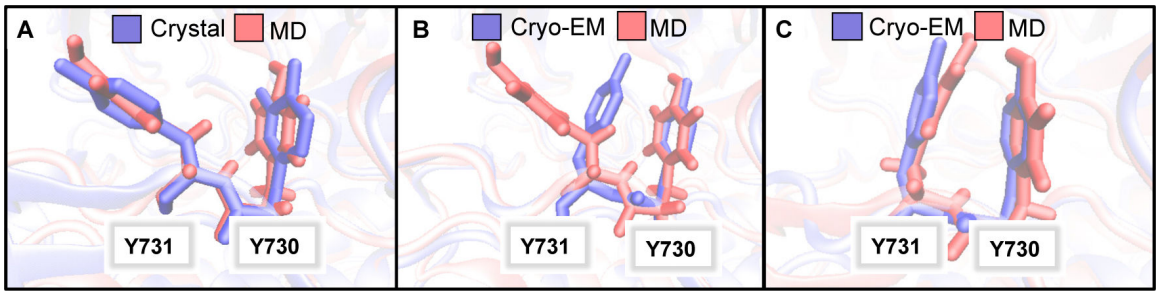

Figure 2.

Superimposition of conformations of Y731/Y730 observed in X-ray crystal or cryo-EM structures with those from the MD simulations. In these figures, the blue coloring represents the X-ray crystal or the cryo-EM structure, whereas the red coloring represents the conformation from the MD simulations. (A) Y-Y dyad in $Y730NH_2$ substituted Class Ia *E. coli* RNR,[41] χ_1 = 188°, and a flipped-out conformation from the MD simulations, χ_1 = 180°,. (B) Y-Y dyad from the cryo-EM structure, χ_1 = 271°, and the same MD conformation from panel A. (C) Y-Y dyad observed in umbrella sampling simulations, χ_1 = 274°, and the cryo-EM structure.

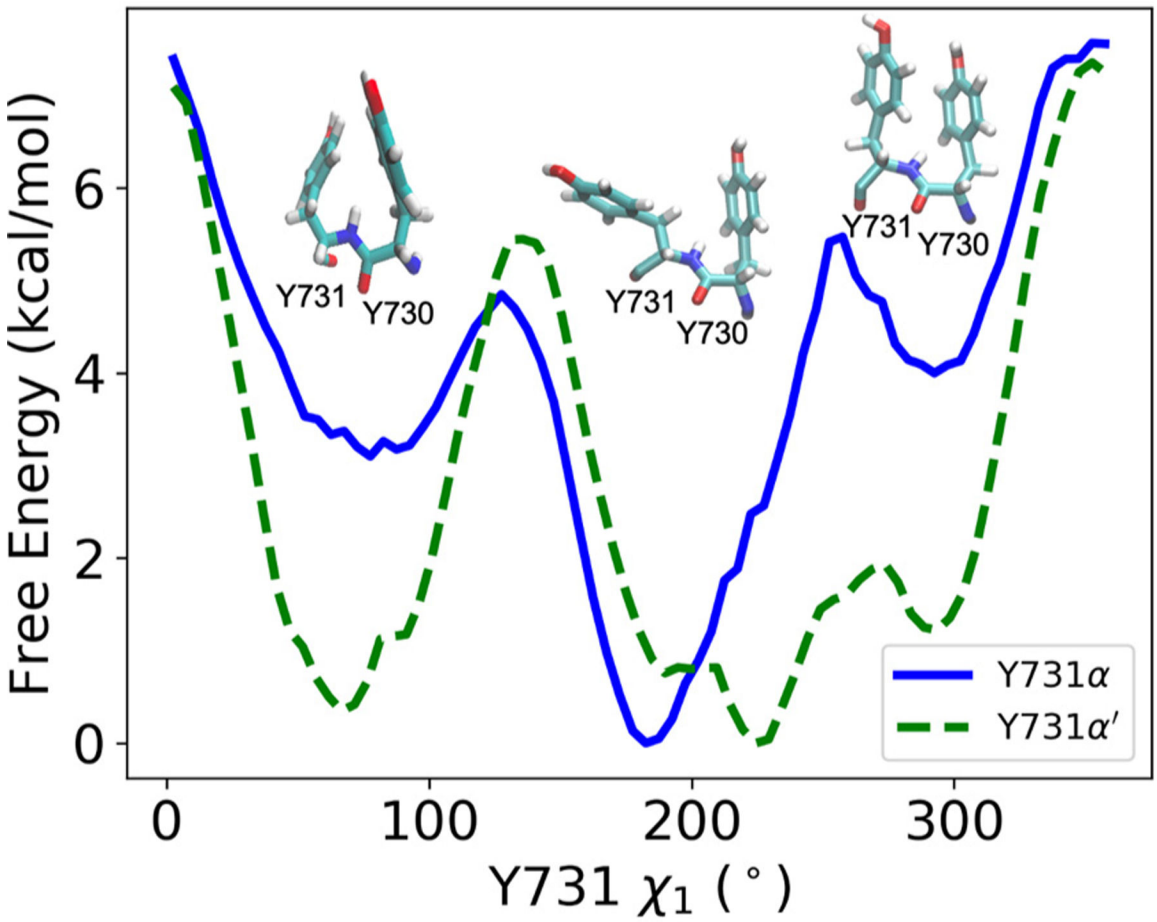

Figure 3.

Free energy profiles of the combined data for the Y731 χ_1 dihedral angle rotation in the α (blue solid) and α′ (green dashed) subunits. The three minima in the Y731α PMF correspond to the off-pathway (χ_1 = 77.5°), flipped-out (χ_1 = 182.5°), and stacked (χ_1 = 292.5°) conformations.

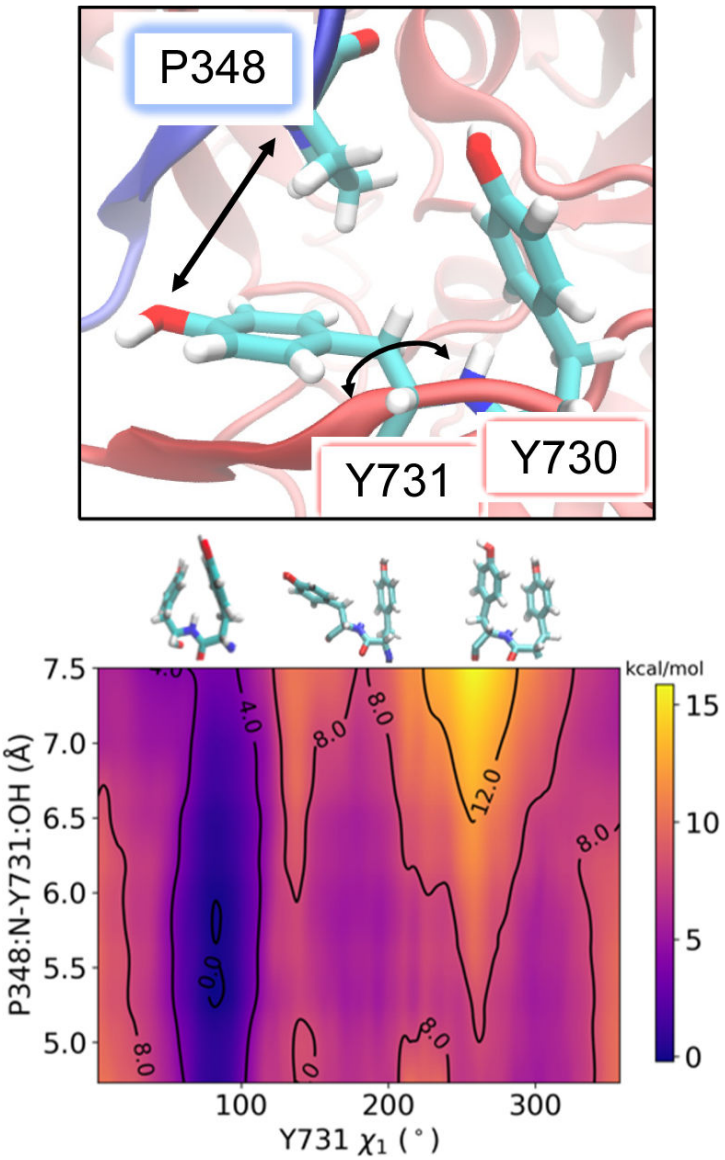

Figure 4.

Reaction coordinates used to generate the 2D PMF (top) and the two-dimensional free energy surface as a function of the Y731 dihedral angle (χ_1) and the P348:N and Y731:OH distance in the α′ subunit (bottom). The full 2D PMF extending to larger distances is given in Fig. S10. The flipped-out and stacked conformations are 5.5 and 5.3 kcal/mol, respectively, higher than the off-pathway conformation, which is likely to be kinetically inaccessible in this RNR.

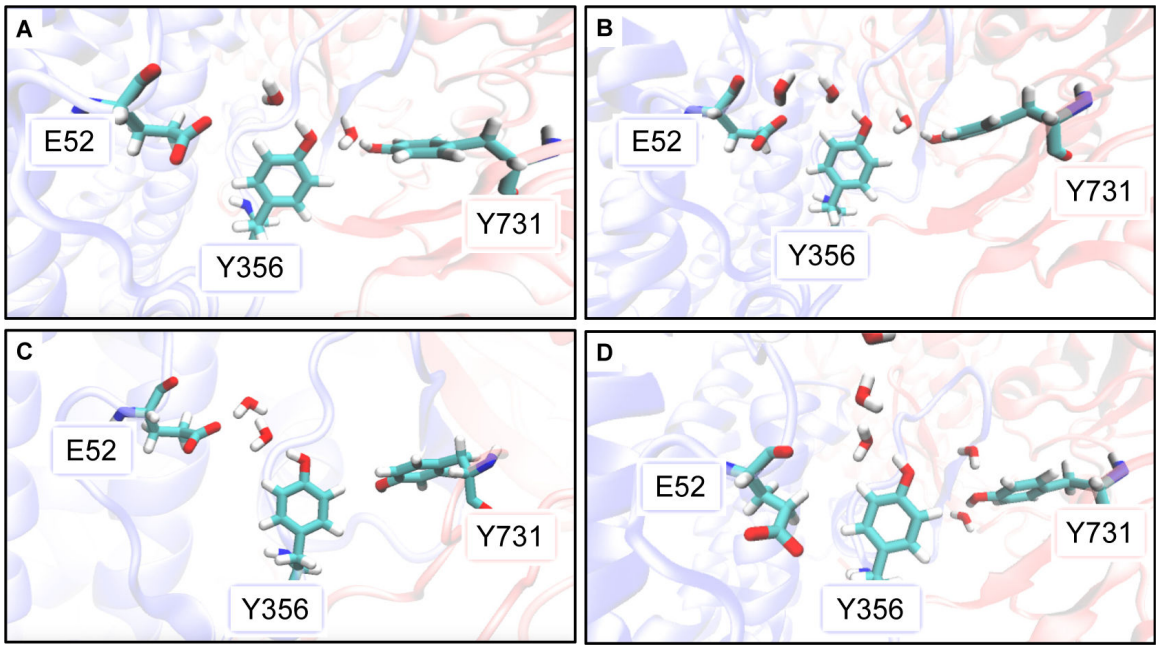

Figure 5.

Conformations depicting the diversity of water configurations at the interfacial region, illustrating (A) two hydrogen bonds of Y356 with water molecules and the sharing of these bridging water molecules with E52 and Y731; (B) bridging water molecule between Y356 and Y731, as well as a network of two water molecules between Y356 and E52; (C) network of two water molecules between Y356 and E52; (D) network of several water molecules from Y356 to bulk water, with Y731 interacting with two other water molecules. Note that Y356 is solvent accessible, and these are only examples of water conformations sampled during the 1.2 μs of MD. An example of Y356 hydrogen bonding with E52 is given in Figure S12.

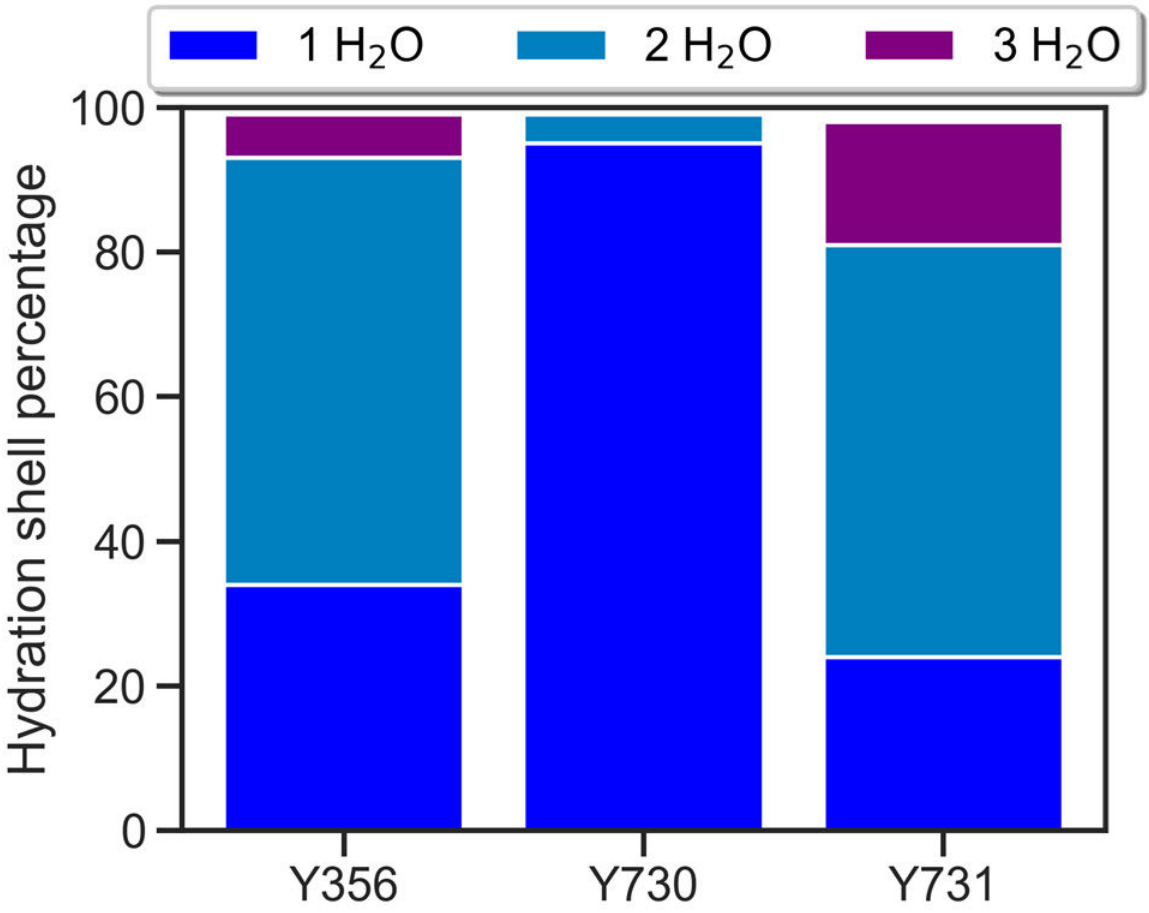

Figure 6.

Percentage of conformations with precisely one, two, or three water molecules with the oxygen atom within 3.4 Å of the specified Y oxygen atom. For each Y, the deviation of the sum of these percentages from 100% is the percentage of conformations with no water molecules within this distance. The percentages were determined from over 120,000 conformations obtained from 1.2 μs of MD, where Y731 was always in the flipped-out conformation.

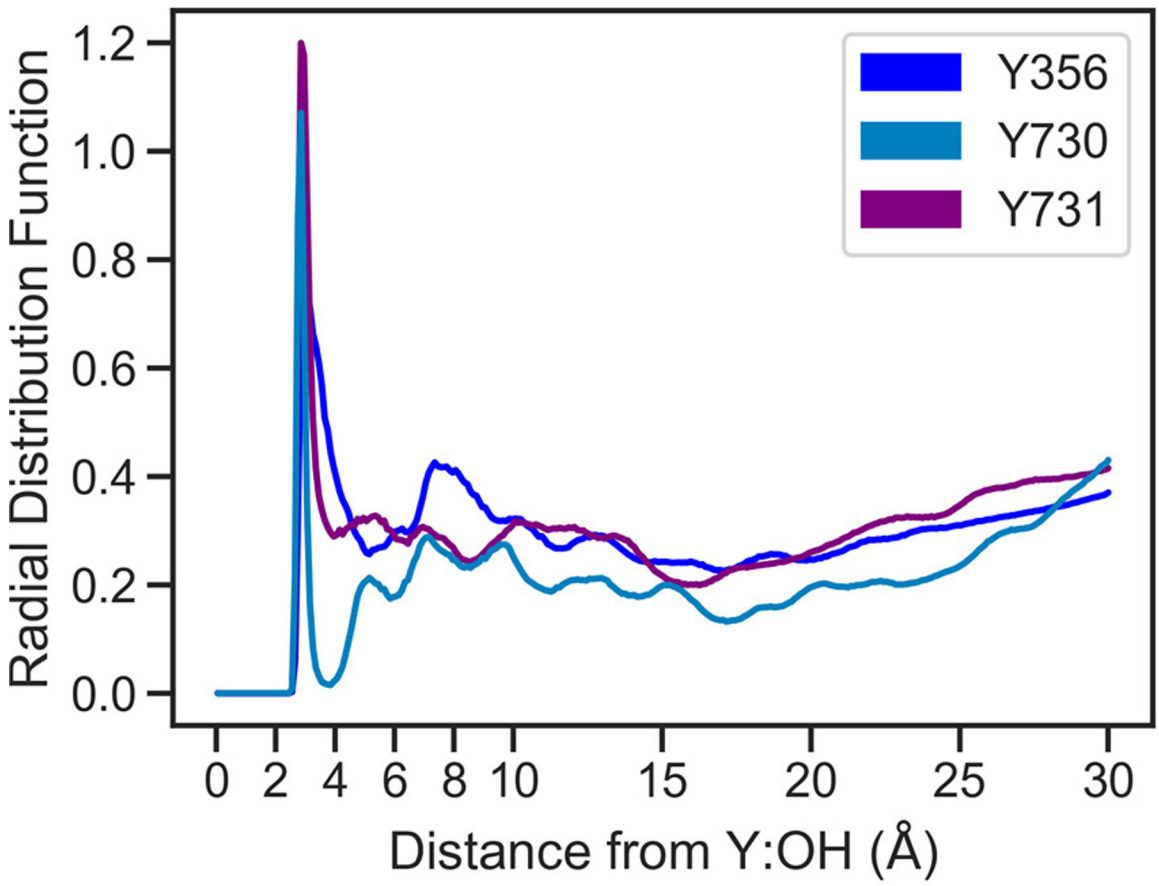

Figure 7.

Radial distribution function (RDF) between the phenolic oxygen of Y356, Y730, or Y731 and surrounding water molecules. The hydration numbers, defined as the average number of water molecules with oxygen atoms within 3.4 Å of the Y oxygen atom, are 1.5, 1.3, and 1.8 for Y356, Y730, and Y731, respectively, where Y731 is in the flipped-out conformation. These radial distribution functions approach unity at longer distances (Figure S13).

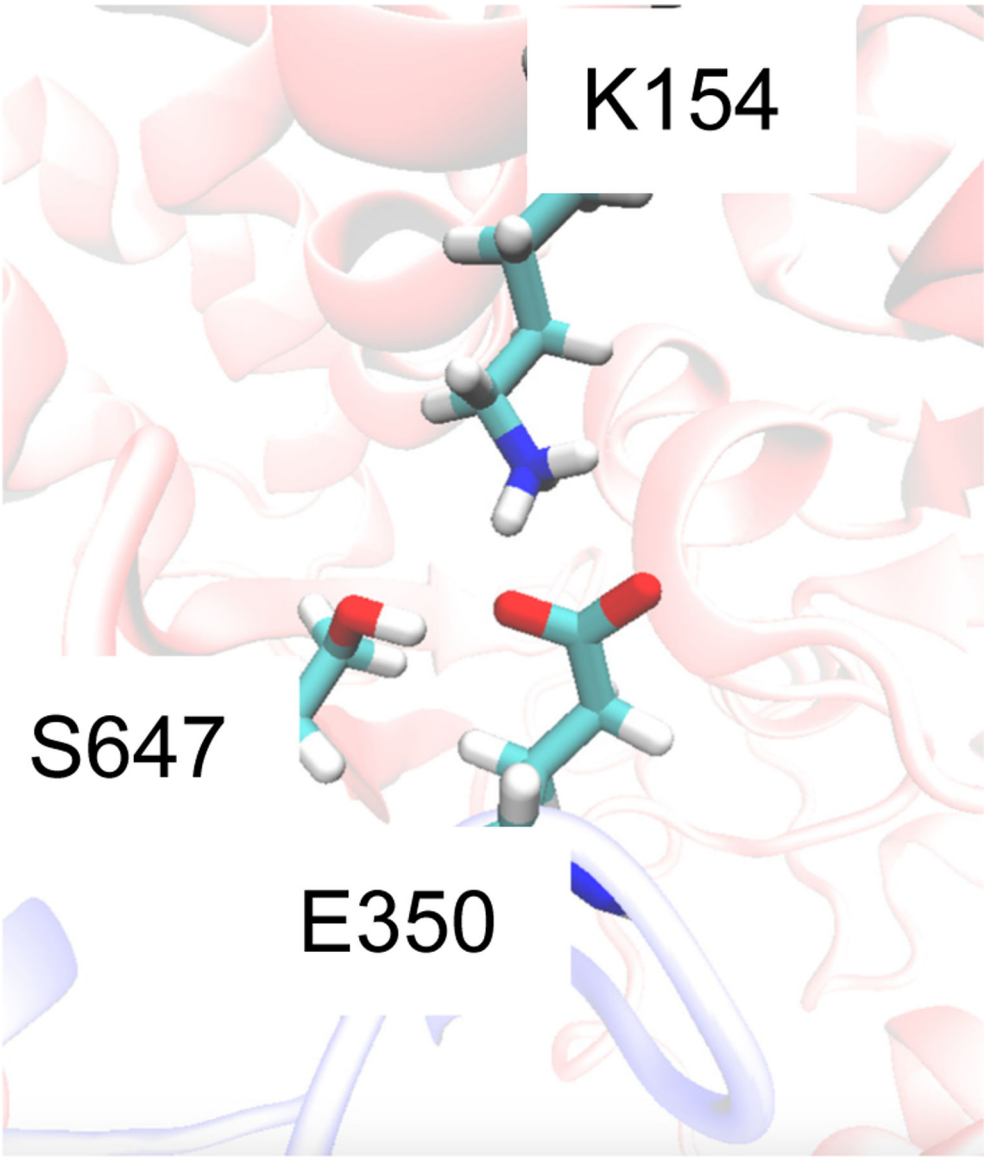

Figure 8.

Interactions of E350β with K154α in a conformation obtained from the MD trajectories. Residues 180–240, 430–460, and 610–640 of α were excluded for visualization purposes. The backbone of α is represented in red, while the backbone of β is represented in blue.

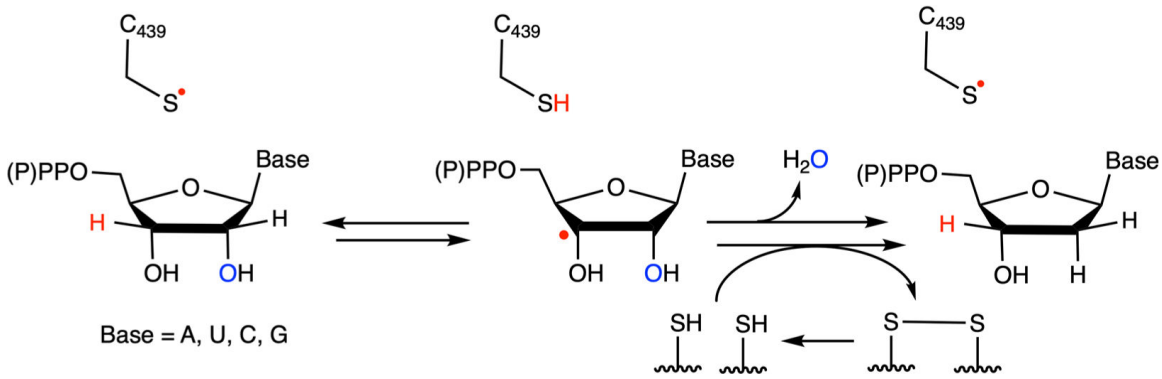

Scheme 1.

Conversion of Nucleoside 5′-Diphosphates (NDPs) or Triphosphates (NTPs) to Deoxynucleotides (dNDP or dNTP) by RNR.

Table 1.

Average Distances with Standard Deviations along PCET Pathway from Cryo-EM Structure and MD Simulations.[a]

System	Y122:O• - W48:NH	Y122O• - Y356:OH	Y356:OH - Y731:OH	Y730:0H - C439:SG[b]	Y122:O• - C439:SG
Cryo-EM	10.0 Å	21.2 Å	8.3 Å	2.8 Å	32.4 Å
MD α2β2	10.2 ± 0.3 Å	20.3 ± 1.1 Å	8.0 ± 1.6 Å	3.5 ± 0.3 Å	32.4 ± 0.6 Å

[a]The distances were averaged over 120,000 conformations obtained from 1.2 μs of MD simulations.

[b]The starting structure used for the MD differed slightly from the deposited structure in having fewer cycles of refinement than the deposited PDB. The RMSD of the C_α atoms in the starting structure for MD compared to the cryo-EM structure is 0.087 Å.